EES Batteries

ROYAL SOCIETY OF CHEMISTRY

PAPER

View Article Online
View Journal | View Issue

Cite this: *EES Batteries*, 2025, **1**, 1267

Tailored electrolyte additive design for suppressing irreversibility in dry-processed anodes and enhancing electrochemical stability in full-cells

Seungmin Han,†[a] Woojin Jeong,†[a] Ryeowon Kang,[b] Minseok Kim,[b] Mikang Jeong,[b] Hyun-Wook Lee,[c] Ye-Jin An,[c] Ho-Jeong Ji,[c] Moonsu Yoon,[b] Patrick Joohyun Kim,[d] Seho Sun,[e] Taeseup Song,[a] Dongsoo Lee,*[b] Won-Jin Kwak*[c] and Junghyun Choi*[b]

Introducing silicone (Si) with high theoretical capacity into dry electrode technology offers potential to dramatically boost the energy density of lithium-ion batteries (LIBs), making them an attractive candidate for next-generation high-energy storage systems for electric vehicles (EVs). However, the continuous volume expansion/contraction of Si during cycling and the irreversible decomposition of polytetrafluoroethylene (PTFE) in the reduction process significantly degrade the interfacial and mechanical stabilities of Si-based dry-processed anodes during cycling. In this study, we introduced fluoroethylene carbonate (FEC) as an electrolyte additive to address these challenges in a dry-processed Si/C–graphite composite (DSG) anode system. This strategy effectively suppressed PTFE decomposition by facilitating the formation of a stable LiF-based solid electrolyte interphase (SEI) layer and alleviated the volume change of DSG anode through improved mechanical properties. In addition, we systematically tailored the concentration of FEC to improve the electrochemical stability at both the anode and cathode while observing the distinct degradation mechanisms occurring at each electrode under excessive FEC addition conditions. The resulting balanced electrolyte additive design enabled a high-performance full-cell using a DSG anode with a high areal capacity of 7.6 mAh cm^{-2}, leading to a high average coulombic efficiency (CE) of 99.9% and high areal capacity of 4.6 mAh cm^{-2} after 300 cycles. These insights into the DSG anode system offer a practical pathway toward high-energy-density LIBs.

Received 23rd May 2025,
Accepted 21st July 2025

DOI: 10.1039/d5eb00100e

rsc.li/EESBatteries

Broader context

In response to the global push for carbon neutrality, electric vehicles (EVs) have emerged as promising solutions to reduce greenhouse gas emissions. Central to EV performance are lithium-ion batteries (LIBs), which determine both the driving range and charging speed. To meet the growing energy demands, silicon-based anodes have attracted attention due to their high theoretical capacity. However, the large volume changes that silicon (Si) undergoes during charge–discharge cycles can lead to electrode degradation and shortened battery lifespan. Additionally, attention has been shifting toward cost-effective and environmentally friendly manufacturing approaches. Dry electrode processing offers a solvent-free alternative, but the polytetrafluoroethylene (PTFE) binder commonly used in dry-processed anodes is prone to electrochemical decomposition, impairing the performance. In this study, we addressed these challenges by incorporating fluoroethylene carbonate (FEC) as an electrolyte additive to enhance the electrode stability. FEC suppressed PTFE decomposition and maintained anode integrity during cycling. It also affected the cathode stability, particularly with an Ni-rich cathode. This study identifies an optimal FEC concentration that stabilizes both electrodes, enabling durable full-cell performance.

[a]*Department of Energy Engineering, Hanyang University, 222 Wangsimni-ro, Seongdong-gu, Seoul, 04763, Republic of Korea*
[b]*School of Chemical, Biological and Battery Engineering, Gachon University, Seongnam-si, Gyeonggi-do, 13120, Republic of Korea. E-mail: junghchoi@gachon.ac.kr, dslee9117@gachon.ac.kr*
[c]*School of Energy and Chemical Engineering, UNIST, Ulsan, 44919, Republic of Korea. E-mail: wjkwak@unist.ac.kr*
[d]*Department of Applied Chemistry, Kyungpook National University, Daegu, 41566, Republic of Korea*
[e]*School of Chemical Engineering, Yeungnam University, Gyeongsan, 38541, Republic of Korea*
†These authors contributed equally to this work.

1. Introduction

Since the industrial revolution, the rapid rise in fossil fuel consumption has led to significantly increased greenhouse gas emissions, driving global warming and climate change.[1,2] In response, carbon neutrality has emerged as a major global priority, with electric vehicles (EVs) positioned as a promising alternative to internal combustion engine vehicles.[3–5] Lithium-ion batteries (LIBs) serve as the primary energy storage system for EVs because of their potential for high energy density and reduced carbon emissions.[6–8] However, conventional LIBs still face critical challenges such as limited driving range and constraints on fast charging capability.[9–11] Therefore, the development of LIBs with higher energy density is becoming increasingly crucial to meet the demands of next-generation energy storage applications.

In recent years, the development of high-capacity active materials and innovative electrode fabrication techniques has attracted increasing attention to overcome the limitations of conventional LIBs.[12,13] From a material perspective, silicon (Si)-based anodes are particularly promising owing to their high theoretical specific capacity of 3579 mAh g^{-1} ($Li_{15}Si_4$), which is nearly 10 times higher than that of graphite (372 mAh g^{-1}, LiC_6).[14,15] However, Si undergoes considerable volume change during lithiation/delithiation, which leads to continuous fracture of the solid electrolyte interphase (SEI) and deteriorated electrode integrity.[16–18] Numerous methods, such as nanosizing, blending with commercial graphite, and employing flexible binders, have been proposed to mitigate these issues.[19–21] Among them, the Si–graphite (Si–G) composite system is considered the most practical approach for enhancing energy density.[22]

In the case of electrode manufacturing process, dry electrode technology is well-suited to fabricate thick film electrodes with high mass loading because it eliminates the undesirable binder migration problem that occurs during the solvent drying processes.[23–25] However, polytetrafluoroethylene (PTFE) induces electrochemical instability in an anodic environment due to its low lowest unoccupied molecular orbital (LUMO).[26–28] This property triggers the decomposition reaction of PTFE by defluorination during the lithiation process, resulting in a low initial coulombic efficiency (ICE) and weakened mechanical properties of the electrode.[29]

In our previous work, we demonstrated that introducing fluoroethylene carbonate (FEC) as an electrolyte additive effectively mitigates both the PTFE decomposition reaction and electrode degradation in dry-processed graphite anodes by forming a stable solid electrolyte interphase (SEI) layer and protecting binder properties.[30] Furthermore, FEC is one of the most commercially utilized electrolyte additives in anodes containing Si, as it forms a stable LiF-based SEI layer at the surface of active materials when applied under an optimal concentration.[31–33] This optimized FEC-derived SEI layer can effectively reduce irreversible capacity loss and mitigate capacity fade, highlighting the potential of FEC additives in supporting the development of dry-processed Si-based anodes for high-energy battery systems.

Although FEC primarily stabilizes the anode interface, its influence can extend to the cathode side, especially in full-cell configurations with a Ni-rich cathode.[34–36] Generally, FEC can generate byproducts that induce the degradation of $LiPF_6$ and promote HF formation, which attacks Ni-rich cathode surfaces.[37–40] In the case of an excessive concentration of FEC, elevated HF attacks can lead to the dissolution of the transition metal (TM), consequently degrading the surface structure. Such cross-talk effects between electrodes underscore the risk of overusing electrolyte additives without proper concentration control. Therefore, an optimized FEC additive system is critical not only for stabilizing the SEI but also for suppressing cathode degradation, ensuring balanced interfacial behavior across both electrodes.

In this study, we systematically analyzed the trade-off between varying FEC concentrations to identify the optimal condition that balances interfacial stability and electrochemical performance in full cells comprising a dry-processed Si/C–graphite composite (DSG) anode and Ni-rich NCM cathodes. The FEC plays a crucial role as a pre-reactive electrolyte additive at the anode, which critically contributes to the formation of a uniform and robust SEI layer. The LiF-based SEI formed on the anode interface protects the active material and effectively suppresses PTFE decomposition during lithiation, thereby improving the ICE and mitigating electrode degradation. In addition, the robust binding network preserved by FEC effectively controls the volume change and enhances the structural stability of the electrode despite the presence of Si. On the cathode side, structural integrity associated with varying FEC concentrations was observed through scanning electron microscopy (SEM), time-of-flight secondary-ion mass spectrometry (TOF-SIMS), and high-resolution transmission electron microscopy (HR-TEM). These analyses revealed that excessive FEC promotes the formation of HF, which induces severe structural deterioration of the Ni-rich cathode surface by accelerating TM dissolution. Consequently, an optimal electrolyte additive system improves the irreversible reaction in DSG anodes while simultaneously mitigating the cathode-side degradation, thereby achieving an outstanding capacity retention of 74.5% and a high average coulombic efficiency (CE) of 99.9% over 300 cycles under high areal loading in full-cell configurations. This optimized guideline for electrolyte additive design offers high potential for the practical implementation of high-performance and high-energy density LIBs.

2. Results and discussion

2.1. Favorable effect of the FA system in DSG anode

Fig. 1 shows the fabrication process of DSG anode and the beneficial effects of the FEC electrolyte additive (FA) in DSG anode compared to a system without FA. DSG anode was fabricated using dry-processed electrode technology of Maxwell type using PTFE binder and employing Si/C–graphite composite as the active material (Fig. 1a). This well-fabricated DSG anode is displayed in Fig. 1b, and the detailed fabrication

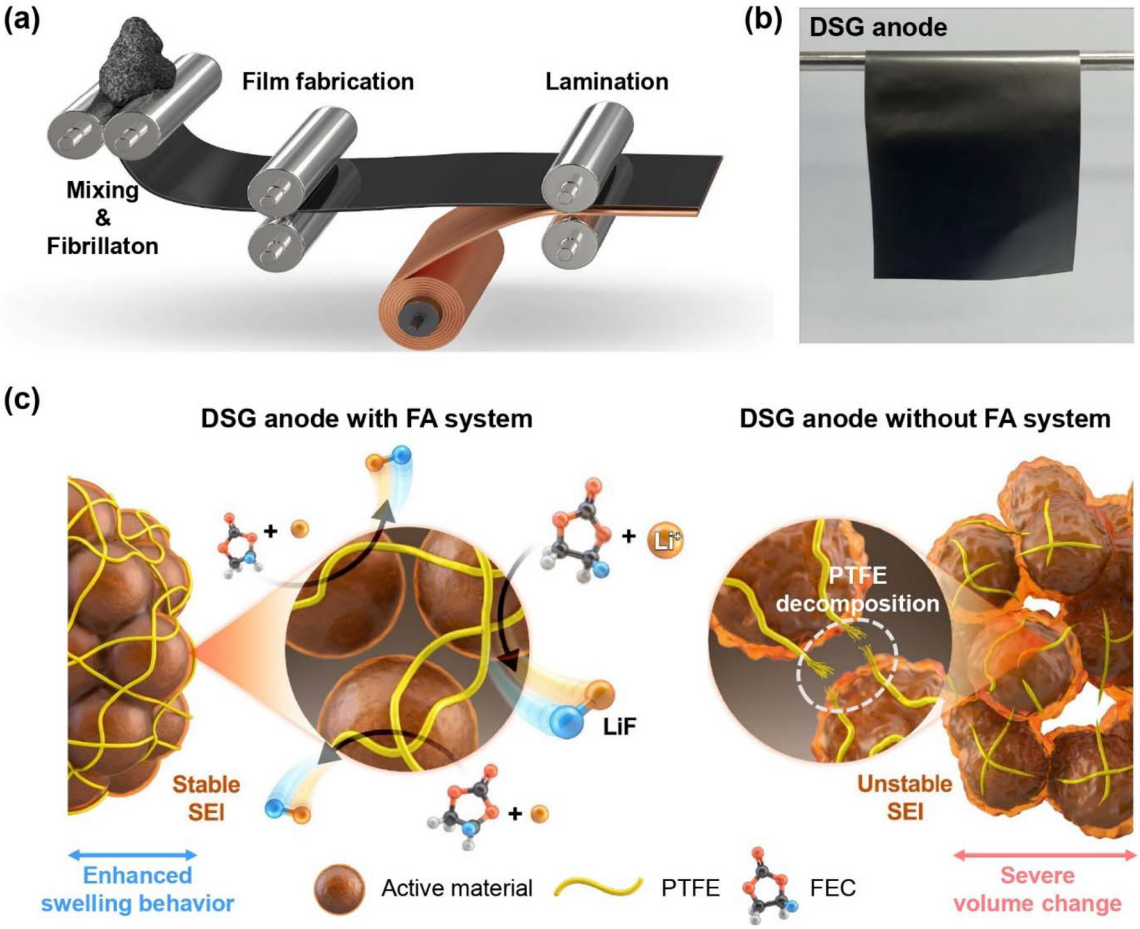

Fig. 1 (a) Schematic of the manufacturing process of DSG anode and effect of the FA system on DSG anode system. (b) Freestanding DSG anode sheet. (c) Schematic of the effect of the FA system on DSG anode.

method is presented in the Experimental section. As illustrated in Fig. 1c, the introduction of FA into DSG anode system plays a crucial role in improving interfacial and mechanical stability. During the initial lithiation process, FA undergoes preferential reductive decomposition prior to polytetrafluoroethylene (PTFE) reduction reaction, leading to the formation of a conformal and stable LiF-based SEI on the surface of the active materials. This passivating SEI layer effectively suppresses the decomposition reaction of PTFE and protectes active materials, mitigating electrode volume changes and improving mechanical properties. Thus, the incorporation of the FA system paves a direct pathway to mitigate irreversibility and enhance electrode durability in LIBs with DSG anodes.

2.2. Characterization of DSG anode in a diverse FA system

FA is effective in DSG anode systems, demonstrating the effect of additive concentration on the anode interface (Fig. 2). PTFE loses its binder functionality owing to its decomposition during the lithiation process, resulting in structural deformation and compromised mechanical integrity of the electrode.[41,42] To address this problem, we previously introduced FA into dry-processed graphite anodes, which suppressed PTFE decomposition, enhanced the mechanical properties, and mitigated the volume change of the electrodes.[30] However, owing to the substantial volume change of Si, Si-containing electrodes are prone to considerable morphological changes, necessitating a reassessment of their structural degradation during cycling.

To confirm whether our strategy was also effective for DSG anodes, we observed the morphological changes in the electrodes (Fig. 2a–c). Fig. S1 shows the electrode morphologies before cycling. The PTFE binders in the electrode formed well-fibrillated chain networks between the active materials, indicating that the dry electrode remained intact. After 1 cycle, the DSG anode without FA exhibited an inhomogeneous distribution and scission of the PTFE binder chains (Fig. 2a). However, the DSG anode with FA maintained the PTFE binder network between the active materials. FA effectively suppressed the PTFE decomposition reaction, even in the dry-processed anode system with Si (Fig. 2b). The swelling ratio of the DSG anode with FA and without FA after cycling was presented to confirm the degradation of PTFE and the electrode, which was inhibited by the introduction of FA (Fig. 2c). Before cycling, DSG anode was 97.0 μm thick (Fig. S2). The well-dispersed Si

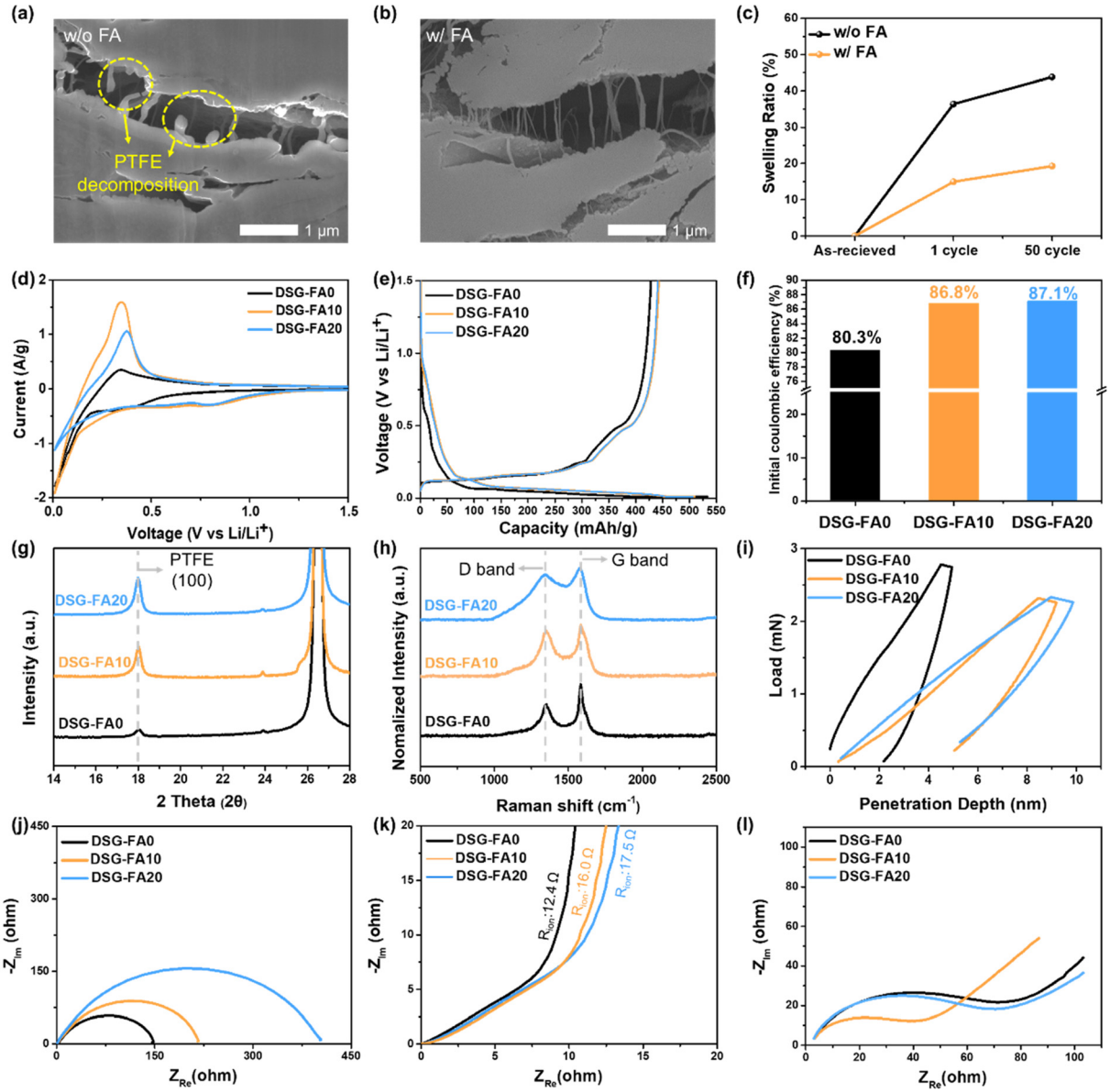

Fig. 2 Characterization of PTFE decomposition and mechanical functionalities of DSG anodes with different FA concentrations. Cross-sectional SEM images of DSG anodes after cycling (a) without and (b) with FA. (c) Electrode swelling ratio before cycling, after 1 cycle and after 50 cycles. Electrochemical analyses of DSG-FA0, DSG-FA10 and DSG-FA20 (d) CV curves, (e) voltage profiles after 1 cycle, and (f) ICE values obtained from first voltage profiles. Comparison of the degree of PTFE decomposition after 1 cycle in DSG-FA0, DSG-FA10 and DSG-FA20. (g) XRD pattern and (h) Raman spectra of DSG-FA0, DSG-FA10 and DSG-FA20. (i) Nanoindentation load–displacement curves for the evaluation of mechanical properties. EIS spectra of (j) ion-blocking cells (k) symmetric cells before cycling and (l) symmetric cells after 1 cycle.

particles in DSG anode are also represented by a brighter color due to their higher atomic number in SEM images utilizing the backscattered electron (BSE) mode. The thickness of the DSG anodes with and without FA after cycling was determined using SEM images (Fig. S3 and S4) and the swelling ratio was calculated by dividing the value of the change in thickness by the original thickness. The DSG anode with FA delivered a lower swelling ratio of 14.8% than the DSG anode without FA (36.5%) after 1 cycle. Similarly, the FA-containing DSG anode exhibited improved swelling behavior of 19.2% after 50 cycles compared to the 43.8% for the DSG anode without FA, despite the stress accumulation from repeated volume expansion/contraction during cycling. These results indicate that FA not only effectively alleviates electrode degradation by suppressing PTFE decomposition and volume expansion of the electrode but is also suitable in DSG anode system. Although the introduction of FA was effective in DSG anode, its addition altered the chemical, mechanical, and electrochemical properties, depending on its concentration.

Various analyses were conducted depending on the concentration of the added FA (Fig. 2d–l). The cyclic voltammetry (CV) curve at a scanning rate of 0.1 mV s^{-1} shows the reduction

region of FA and PTFE (Fig. 2d). For the DSG anode without FA (DSG-FA0), the decomposition peak of PTFE was observed in the range 0.3–0.6 V. In both DSG anodes with 10 wt% FEC and 20 wt% FEC (DSG-FA10 and DSG-FA20, respectively), the reduction peaks attributed to the decomposition reaction of FA were preferentially generated at 0.8 V. Additionally, the PTFE reduction peak was not represented in the same voltage range of 0.3–0.6 V in both samples. Thus, the FEC-derived SEI by FA mitigates the decomposition of PTFE. Fig. 2e illustrates the initial voltage profiles of DSG-FA0, DSG-FA10, and DSG-FA20. DSG-FA10 and DSG-FA20 deliver reduced irreversible capacity of 66.8 mAh g^{-1} and 65.2 mAh g^{-1}, compared to 104.9 mAh g^{-1} of DSG-FA0. This is attributed to the suppression of PTFE decomposition. Fig. 2f shows the ICE values obtained from the first voltage profile. Although the ICE of DSG-FA20 was slightly improved compared with that of DSG-FA10, no noticeable difference was observed. Therefore, once sufficient FEC-derived SEI is formed on the surface of the active material, the suppression of PTFE decomposition does not increase significantly. In addition, to evaluate the effect of reducing the additive concentration below 10 wt%, an additional experiment using 5 wt% FEC (FA5) was performed, as presented in Fig. S5. As a result, the ICE of DSG-FA5 was improved from 80.3% for DSG-FA0 to 83.4%, and the irreversible capacity was reduced from 104.9 mAh g^{-1} to 86.5 mAh g^{-1}. However, FA5 is not the optimal concentration for DSG anode compared to DSG-FA10 and DSG-FA20 due to its relatively limited improvement in suppressing PTFE decomposition. XRD and Raman analyses were conducted to more clearly observe the difference in PTFE decomposition depending on the FA concentration (Fig. 2g and f). The results of DSG anodes before cycling are shown in Fig. S6 and S7, respectively. After 1 cycle, FA10 and FA20 exhibited a more distinct (100) plane peak for PTFE than FA0. The structural deformation of PTFE was suppressed by the alleviation of PTFE degradation (Fig. 2g). Similar results were obtained for the Raman spectra and I_D/I_G ratios (Fig. 2h and Table S1). The asymmetric intensity increased significantly owing to PTFE decomposition in FA0, resulting in a reduced I_D/I_G ratio of 0.6. However, DSG-FA10 and DSG-FA20 exhibited less change in the I_D/I_G ratio owing to the reduction in the structural changes of PTFE. Fig. 2i and Table S2 show the mechanical properties measured using nanoindentation analysis. No significant differences in mechanical properties were observed between DSG-FA10 and DSG-FA20, although both showed notable improvement compared to DSG-FA0. Consequently, a sufficient concentration of FA effectively suppressed the decomposition reaction of PTFE, and no significant additional improvement was observed in DSG anode beyond this concentration.

However, an excessive electrolyte additive increases the viscosity of the electrolyte, thereby reducing Li-ion mobility and electrochemical performance[43] Therefore, identifying the trade-off relationship depending on the concentration of the electrolyte additive and optimizing the electrolyte system is crucial. To determine whether the increase in FA concentration affected Li-ion mobility, ion-blocking cells were fabricated, and electrochemical impedance spectroscopy (EIS) analysis was performed after cell assembly (Fig. 2j). The resistance of DSG anode increased as the electrolyte concentration increased. This result is in agreement with the measurements of the Li-ion migration resistance (R_{ion}) before cycling (Fig. 2k). The DSG-FA20 exhibited the largest value of 17.5 Ω, indicating that excessive FA could interrupt Li-ion transport in DSG anode system. Furthermore, to determine the electrode degradation caused by the decomposition reaction of PTFE and its influence on the electrolyte additive concentration, symmetric cells were fabricated with the retrieved electrodes after 1 cycle, and EIS analysis was performed (Fig. 2l). DSG-FA10 showed the smallest semicircle, indicating the lowest resistance values despite the increased viscosity of the electrolyte. This was attributed to the improved migration of Li ions through the stable FEC-derived SEI layer formed by FA. Although the introduction of FA is suitable for DSG anodes, excessive addition can negatively affect Li-ion mobility. These observations suggest that FA10 is the optimal additive concentration for DSG anode systems.

2.3. Electrochemical performances of half-cells & surface characterization

To investigate the differences in electrochemical performance and interfacial changes at the anode with the addition of FA, we conducted additional analyses (Fig. 3). Fig. 3a shows the electrochemical performance of DSG-FA0, DSG-FA10, and DSG-FA20 at a 0.3 C-rate. FA10 showed improved cycle retention and the highest average CE of 99.7% compared to DSG-FA0 (99.2%) and DSG-FA20 (99.6%). This is because an appropriate additive concentration forms a stable FEC-derived SEI, which not only suppresses PTFE decomposition but also ensures sufficient Li-ion transport. To further support these results on electrochemical performance, EIS analysis was conducted after 50 cycles. In the equivalent circuit model (Fig. S8), the first semicircle is associated with the SEI layer resistance (R_{SEI}), and the second semicircle corresponds to the charge transfer resistance (R_{ct}). Fig. 3c shows the corresponding values. The R_{ct} values of all samples did not differ significantly. However, DSG-FA10 exhibited the lowest R_{SEI} value compared to DSG-FA0 and DSG-FA20. Thus, the formation of a stable and thin LiF-based SEI from FEC decomposition facilitated Li-ion transport. XPS analysis was conducted to investigate the degree of PTFE decomposition and SEI formation at the anode interface. In the F 1s spectrum, the peak at 689.3 eV was assigned to PTFE of the dry-processed anode before cycling (Fig. S9). For DSG-FA0, the PTFE peak was significantly reduced, and peaks corresponding to LiF and $LiP_xF_yO_z$ appeared at 685.3 eV and 686.4 eV, respectively (Fig. 3d). Therefore, the absence of FA accelerated the defluorination of PTFE, thereby causing severe electrolyte decomposition and irreversible reactions. However, both dry-processed anodes using FA exhibited less reduction in the PTFE peak because the degradation of PTFE was mitigated (Fig. 3e and f). Additionally, it is noteworthy that the intensity of the LiF peak was greater in DSG-FA20 than in DSG-FA10. From previous

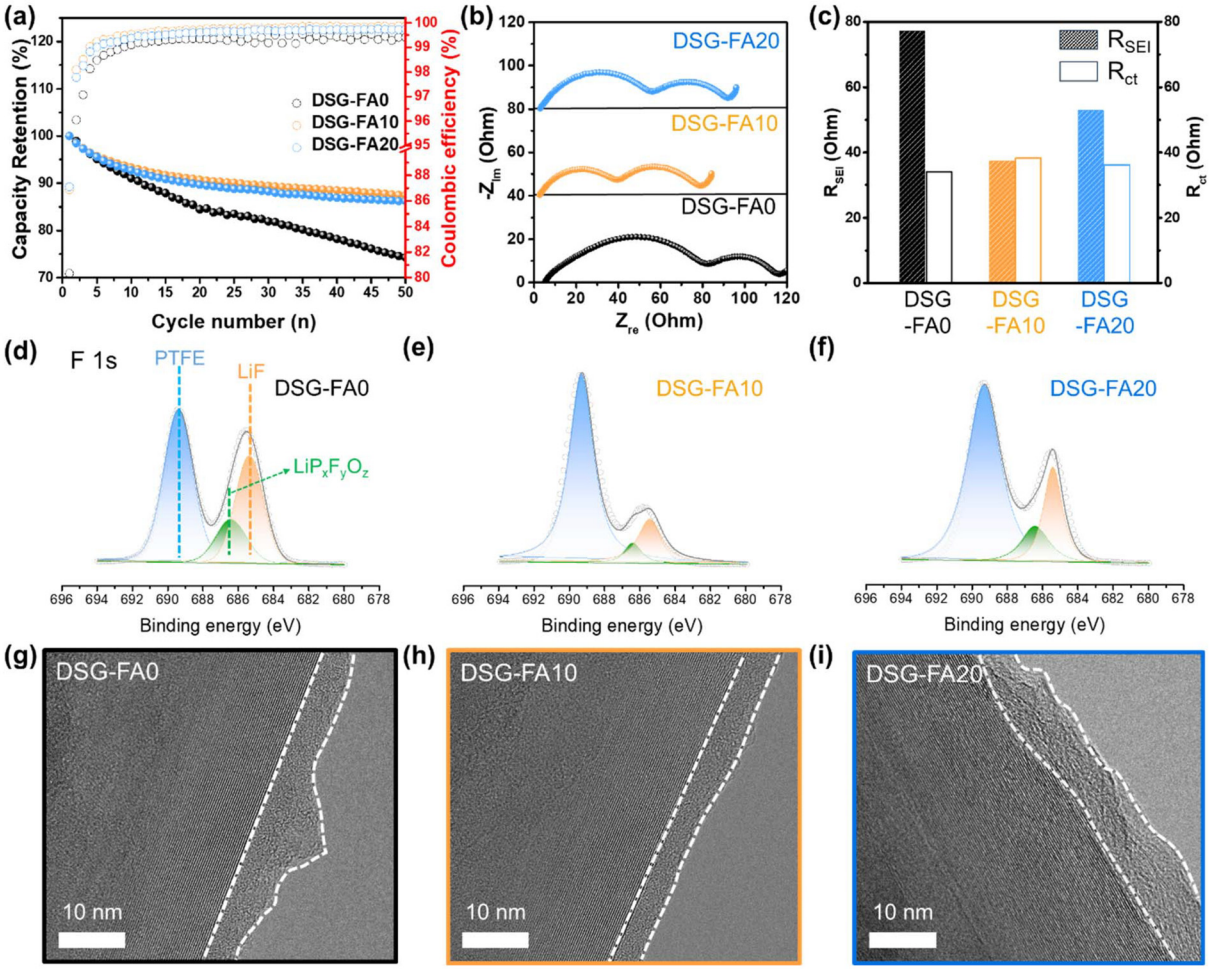

Fig. 3 Electrochemical performances of half-cells using DSG-FA0, DSG-FA10 and DSG-FA20 anodes. (a) Cycling performances for 50 cycles. (b) Nyquist plots after 50 cycles (c) R_{SEI} and R_{ct} values corresponding to the EIS results. F 1s XPS spectra of (d) DSG-FA0, (e) DSG-FA10 and (f) DSG-FA20 after 50 cycles. TEM images of the dry-processed anode surface of (g) DSG-FA0, (h) DSG-FA10 and (i) DSG-FA20 after 50 cycles.

analyses, it was clarified that there was little difference between DSG-FA10 and DSG-FA20 in suppressing PTFE decomposition. Therefore, the increased intensity of the LiF peak suggests that excessive FA leads to an excessively thick LiF-based SEI layer, which hinders Li-ion transport. This interpretation is consistent with the degraded electrochemical performances, as shown in Fig. 3a–c. TEM analysis was performed to further validate the interfacial changes at the anodes (Fig. 3g–i). DSG-FA0 and DSG-FA20 exhibited irregular and thick SEI morphologies, respectively, whereas FA10 exhibited a thin and uniform SEI. These results indicate that a stable and thin LiF-based SEI formed under optimized FA conditions can simultaneously prevent electrode degradation from PTFE decomposition and improve the resistance through enhanced Li-ion kinetics.

2.4. Electrochemical performance of full-cells

FA is commonly recognized as an additive that facilitates the formation of a stable CEI on the cathode while simultaneously inducing HF attack.[44–46] These contradictory characteristics imply that the influence of FA concentration should be considered for both the anode and the cathode. Accordingly, we conducted full-cell tests to understand the influence of anode degradation on cathode performance and to elucidate the role of FA on the cathode side (Fig. 4). Full cells were fabricated with an N/P ratio of 1.1 and their long-term cycling stability was assessed at 0.2 C-rate in the voltage range of 2.8–4.25 V. Fig. 4a–c represent the voltage profiles of the full-cells using Ni-rich NCM electrodes paired with FA0, FA10, and FA20 (NCM||DSG-FA0, NCM||DSG-FA10, and NCM||DSG-FA20, respectively) during 300 cycles. NCM||DSG-FA0 exhibits the largest decrease in reversible discharge capacity of 4.2 mAh cm^{-2} compared to NCM||DSG-FA10 (2.1 mAh cm^{-2}) and NCM||DSG-FA20 (3.3 mAh cm^{-2}) after 300 cycles. This is attributed to severe electrode degradation by the irreversible decomposition reaction of PTFE in the dry-processed anode system, leading to an unstable CE and rapid capacity fading for a full cell with a Ni-rich NCM cathode. Fig. 4d shows the corresponding cycle performances, along with the voltage profiles of NCM||DSG-FA0, NCM||DSG-FA10, and NCM||DSG-FA20 over

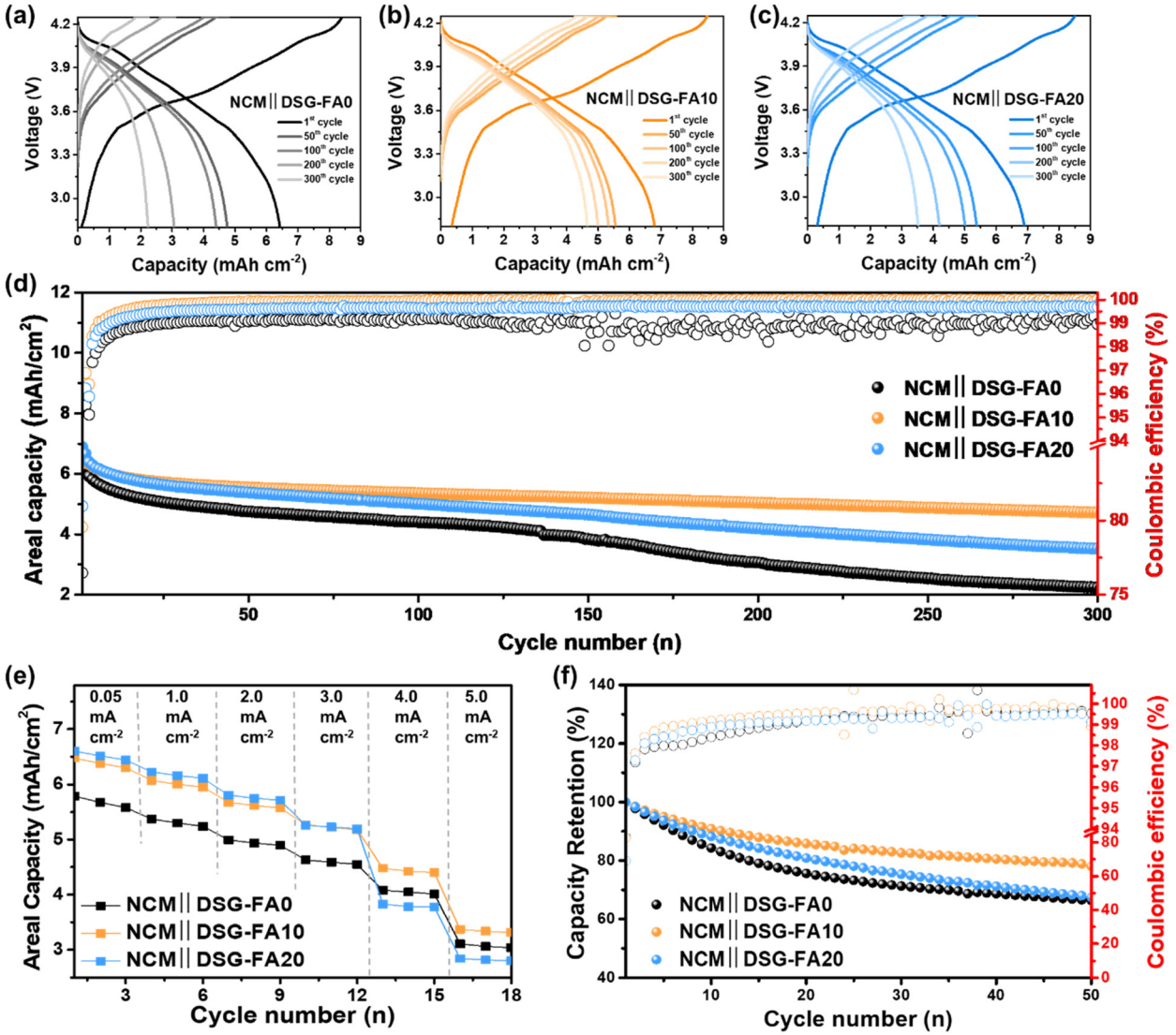

Fig. 4 Electrochemical performances of full cells under a cathode areal capacity of 6.7 mAh cm^{-2} (anode areal capacity of 7.6 mAh cm^{-2}) with different FA concentrations. Voltage profiles over multiple cycles for (a) NCM||DSG-FA0, (b) NCM||DSG-FA10, and (c) NCM||DSG-FA20 anodes. (d) Long-term cycling performances up to 300 cycles at 0.2 C-rate. (e) Rate capabilities measured from 0.05 to 5.0 mA cm^{-2}. (f) High-rate cycling stability for 50 cycles at 2.0 C-rate.

300 cycles. Compared to the half-cell results shown in Fig. 3a, the results of the NCM||DSG-FA20 cell indicated more accelerated capacity fading than those of the NCM||DSG-FA10 cell as cycling progressed. In half-cell configurations, employing Li metal as the counter electrode ensures an abundant supply of Li ions, rendering them less sensitive to irreversible loss of Li ions. In contrast, full cells have a limited Li-ion inventory defined by the cathode. Thus, in the full cell, the excessive FA simultaneously affects cathode degradation by causing a continuous loss of Li ions and generating a large amount of HF that promotes surface degradation. On the other hand, NCM|| DSG-FA10 exhibits stable cycling performance with a high average CE of 99.9% and a high areal capacity of 4.7 mAh cm^{-2} after 300 cycles by enhancing the interface stability of both the DSG anode and Ni-rich NCM under an optimized FA system. This system demonstrates improved electrochemical performance compared to prior literature on dry-processed graphite or carbon anodes, despite using a silicon-containing dry-processed anode (Table S3).

To further examine the influence of the additive concentration on Li-ion kinetics in full-cell systems, we conducted rate capability tests at varying current densities (Fig. 4e). At low current densities (0.05–2.0 mA cm^{-2}), FA10 and FA20 exhibited comparable performances. However, FA20 exhibited a pronounced capacity drop at a high current density of 4.0 mA cm^{-2}, whereas FA10 retained relatively stable performance. Also, Fig. 4f exhibits the cycling stability of the full cells under high-rate (2.0 C-rate) conditions over 50 cycles. The capacity retentions of NCM||DSG-FA0, NCM||DSG-FA10, and NCM||DSG-FA20 after 50 cycles were 66.3, 78.0, and 67.4%,

respectively. Consistent with the rate capability results, NCM||DSG-FA20 showed significantly inferior electrochemical performance compared to NCM||DSG-FA10. These results denote that the elevated additive concentration in FA20 hinders Li-ion transport under high-rate conditions, which is attributed to increased electrolyte viscosity and the formation of a resistive interfacial layer at both electrodes. Additionally, a dry-processed anode with a high Si content (Si/C : Graphite =

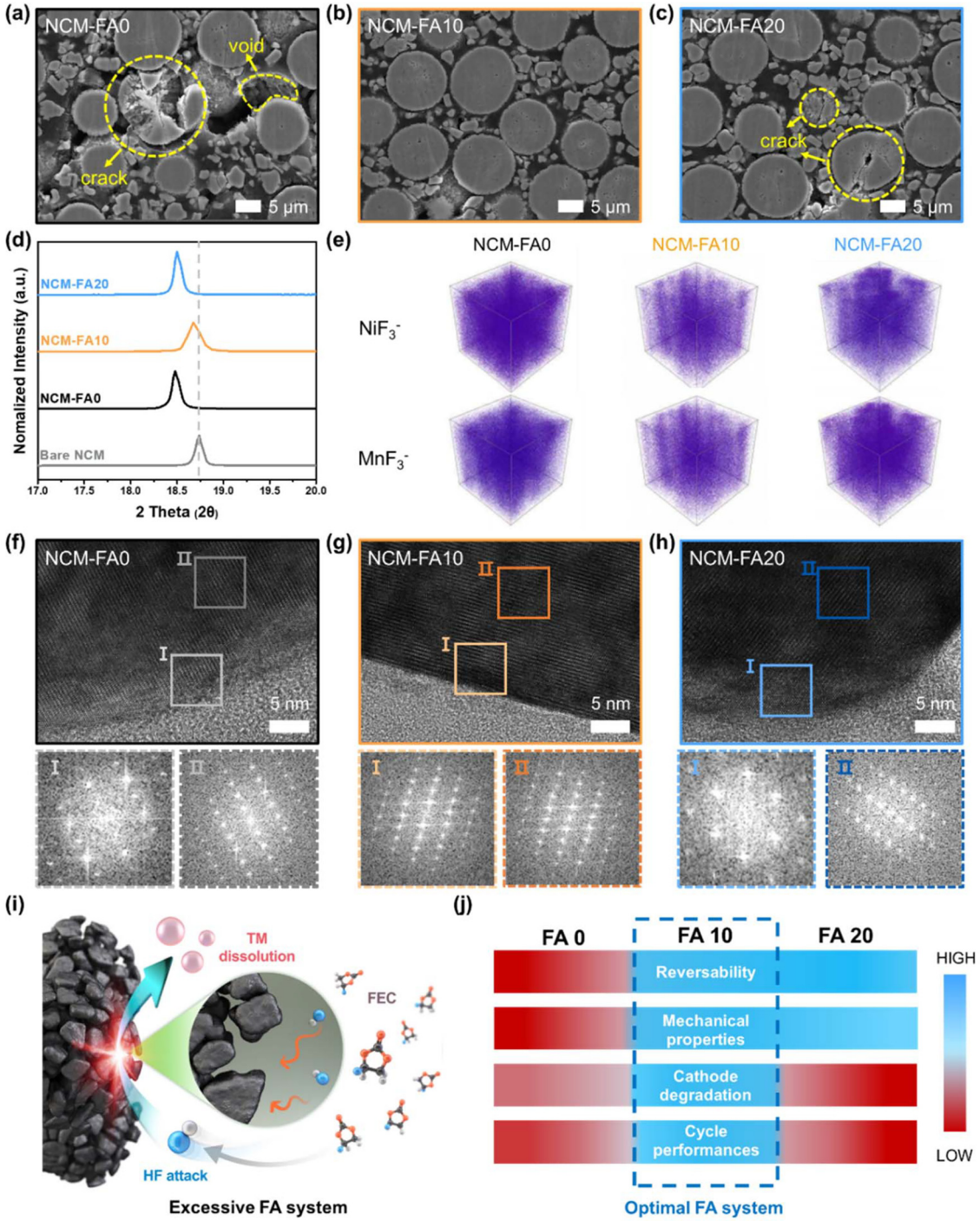

Fig. 5 Structural and interfacial analysis of Ni-rich NCM retrieved from NCM||DSG full cells after cycling. (a–c) Cross-sectional SEM images of NCM-FA0, NCM-FA10, and NCM-FA20 after 100 cycles and (d) XRD patterns after 100 cycles. (e) 3D TOF-SIMS depth profiles visualizing the distribution of NiF_3^- and MnF_3^- species on the Ni-rich NCM cathodes after 300 cycles. TEM and FFT images after 300 cycles of (f) NCM-FA0, (g) NCM-FA10 and (h) NCM-FA20. (i) Schematic of cathode degradation in excessive FA systems. (j) Summary scheme for primary characterization of DSG and NCM||DSG using diverse FA systems.

20 : 80 wt%) was evaluated at a 0.2 C-rate to validate the compatibility of the FA system under more challenging conditions. As shown in Fig. S10, even with increased Si loading, a high initial areal capacity of approximately 6.5 mAh cm^{-2} was achieved and maintained with about 80% of discharge capacity retention after 100 cycles. These results demonstrate that FA10 is suitable even under high areal capacity and high-stress conditions, highlighting its broad applicability as an optimized electrolyte additive formulation for high-energy density DSG anode systems.

2.5. Post-mortem analyses of Ni-rich cathodes

Various analyses were performed to investigate the influence of excess FA on the cathode and the structural degradation of the NCM particles (Fig. 5). Before cycling, the NCM electrode exhibited uniformly distributed active materials with a crack-free morphology (Fig. S11). Fig. 5a–c presents the cross-sectional SEM images of NCM electrodes after 100 cycles with different additive concentrations. The Ni-rich NCM cathode in the FA10 system (NCM-FA10) maintained a crack-free structure after cycling. However, the internal stresses accumulated during the electrochemical cycling of Ni-rich NCM electrodes in the FA0 and FA20 systems (NCM-FA0 and NCM-FA20, respectively) triggered microcracks along the grain boundaries of the particles, as well as voids caused by the rupture of electrodes. Additionally, top-view SEM images of NCM-FA0, NCM-FA10, and NCM-FA20 after cycling also confirmed results consistent with the cross-sectional SEM observations (Fig. S12). Further analyses were conducted to more precisely evaluate the degradation of the cathode. Fig. 5d shows the X-ray diffraction (XRD) results before and after cycling. As reported in previous studies, an HF attack occurring at the cathode can induce structural changes and shift the (003) peak position.[47,48] NCM-FA10 exhibited less peak shift compared with the other samples, indicating the mitigation of crystallographic deformation. From another perspective, NCM-FA20 exhibited a peak position similar to NCM-FA0, where the most severe performance degradation was observed. This result suggests that excessive FA promotes HF generation, leading to HF attack and subsequent structural degradation of the cathode. TOF-SIMS and HR-TEM were carried out to ascertain whether the HF generated by excess FA causes TM dissolution and structural degradation on the surface of NCM particles (Fig. 5e–h). Fig. 5e and Fig. S13 exhibit the 3D depth distribution and normalized intensity of selected fragments for NCM-FA0, NCM-FA10, and NCM-FA20. NCM-FA20 exhibited a greater TM fluoride (NiF_3^- and MnF_3^-) formation compared to FA10, indicating that a higher concentration of HF generated in the FA-rich system aggressively attacked the cathode surface and accelerated TM dissolution. The XPS spectra before and after 300 cycles were also presented to confirm gas evolution by cathode degradation (Fig. S14). In P 2p, the Li_xPF_y and $Li_xPO_yF_z$ peaks were observed at 136.4 and 133.9 eV, respectively. These peaks decreased in NCM-FA10 compared to other samples, suggesting that the FA-10 system could mitigate electrolyte decomposition and HF-related cathode degradation through a finely controlled electrolyte additive strategy.[49] It is inferred to mitigate gas evolution.[50] Additionally, HR-TEM analysis as a visual inspection technique was introduced to further confirm the structural degradation of the cathode. The NCM-FA0 exhibited severe structural collapse at the surface of NCM particles, clearly showing a rock salt structure (Fig. 5f). The corresponding fast Fourier transform (FFT) images indicate crystallographic defects in the regions marked I and II, suggesting significant surface degradation due to electrode deterioration by the HF attack. Likewise, NCM-F20 also displayed a rock salt structure at the surface, as shown in the FFT images of region I (Fig. 5h). These results indicate that excessive FA can trigger undesired structural deterioration by intensification of the HF attack phenomenon. In contrast, the NCM-F10 (Fig. 5g) maintained a more intact surface structure with clear lattice fringes even after cycling. The FFT patterns in regions I and II of NCM-FA10 confirm the preservation of the layered structure of NCM, indicating that the electrode degradation was effectively mitigated by the optimized FA10 system. The schematic illustration highlights cathode degradation in an excessive FA system, where the increase of FA can accelerate cathode degradation by causing a large number of the HF attack on surfaces of cathode (Fig. 5i). Ultimately, the summarized scheme across both the anode and cathode sides confirmed that an insufficient FA content induces severe degradation and poor electrochemical performances at the anode, while excessive FA content triggers notable structural degradation at the cathode (Fig. 5j). By designing an optimized FA concentration system, we provide useful guidance for high-energy-density LIBs with DSG anode system.

3. Conclusion

In this study, we developed a tailored electrolyte design for DSG anode and full cell with a Ni-rich NCM cathode by balancing the concentration of FEC as an electrolyte additive. This strategy inhibited the undesirable PTFE decomposition and reduced the volume expansion/construction in DSG anode system by forming a conformal FEC-derived SEI layer, thereby improving ICE and protecting binder networking. Furthermore, diverse post-mortem analyses revealed that excess FA facilitates HF formation, accelerating TM dissolution and crystallographic defects at the cathode interface. This approach, which involves degradation mechanisms dependent on the increase of FA at both electrodes, demonstrated that an optimized FA10 system provides a suitable balance in DSG and full-cell using a Ni-rich cathode. As a result, a full-cell using a DSG anode with a high areal capacity of 7.6 mAh cm^{-2} exhibited a high average CE and stable long-term cycling performance during 300 cycles. Furthermore, a full-cell with a high Si-containing dry-processed anode exhibited good cycle retention, approximately 80% after 100 cycles. Thus, this optimal FA design for DSG anode system serves as a viable breakthrough for next-generation high-energy LIBs.

4. Experimental section

4.1 Electrode preparation

The dry-processed anode was prepared by blending a silicon–carbon (Si/C) composite with artificial graphite (G49, Shanshan) at a weight ratio of 9 : 91. Carbon black (Super-P) and polytetrafluoroethylene (PTFE, F-104, DAIKIN Industries) were incorporated as the conductive additive and binder, respectively, with the overall composition adjusted to a mass ratio of 96 : 1 : 3 for the active material, carbon black, and binder. The mixture was homogenized using a planetary mixer (ARE-310, Thinky), followed by a vortex mixer (VM-10, WiseMix) to ensure uniform dispersion of all components. The resulting powder blend was then manually kneaded with a mortar and pestle to induce PTFE fibrillation and form a cohesive sheet. This sheet was subsequently calendered using a roll-to-roll machine to achieve the desired thickness and mechanical integrity, yielding a freestanding dry electrode. The electrode film was then laminated onto a pretreated copper (Cu) foil and further compressed to achieve a mass loading of 14.7 mg cm^{-2}, corresponding to an areal capacity of 6.0 mAh cm^{-2}. After calendering, the electrode thickness and density (excluding the Cu foil) were approximately 97 μm and 1.61 g cm^{-3}, respectively.

4.2 Cell assembly

All coin-type cells (CR2032, Wellcos Corporation) were assembled in a dry room with a dew point maintained below −65 °C. All electrodes were dried in a vacuum oven at 100 °C for 3 hours prior to cell assembly to ensure the removal of residual moisture. A polyethylene separator was used in every configuration. For half-cell measurements, lithium metal foil (1.0 T) was used as the counter electrode to assess the electrochemical performance of the dry-processed anodes. In the full-cell configuration, the Si/C–graphite composite anodes were paired with NCM cathodes, with the N/P ratio (capacity-based) set to 1.1. The cathode composition consisted of NCM, carbon black, and binder in a weight ratio of 90 : 5 : 5. A common electrolyte was used in both half- and full-cell experiments, consisting of 1.15 M $LiPF_6$ dissolved in a ternary solvent mixture of ethylene carbonate (EC), ethyl methyl carbonate (EMC), and diethyl carbonate (DEC) in a 2 : 4 : 4 volume ratio. Vinylene carbonate (VC, 1 wt%) was added to all formulations as a stabilizing additive. To investigate the effect of fluoroethylene carbonate (FEC), it was additionally introduced at concentrations of 0, 10, and 20 wt% to prepare FA0, FA10, and FA20 electrolytes, respectively. An electrolyte volume of 200 μL was added to each half-cell and full-cell using a micropipette to ensure precise and consistent dispensing.

4.3. Electrochemical measurements

The electrochemical properties of the coin-type half-cells were assessed through galvanostatic charge–discharge cycling using a battery test system (MIHW-200-160CH-B, NEWARE) following a constant current–constant voltage (CC–CV) protocol. The half-cells underwent two initial formation cycles at 0.1 C and 0.2 C-rate, respectively, followed by continuous cycling at 0.3 C-rate within a voltage window of 0.01–1.5 V *vs.* Li/Li^+. Cyclic voltammetry (CV) measurements were conducted using a potentiostat (VSP, Biologic) at a scan rate of 0.1 mV s^{-1} over the same potential range. Electrochemical impedance spectroscopy (EIS) was performed using a Biologic VSP potentiostat by applying a sinusoidal voltage of 5 mV over a frequency range from 250 kHz to 10 mHz. In addition, symmetric coin cells composed of identical electrodes were assembled to evaluate the Li-ion transport resistance (R_{ion}). These measurements were performed in the 1 Hz to 1 MHz range with an excitation amplitude of 10 mV. For full-cell tests, Si/C–G composite anodes were paired with NCM cathodes. After two formation cycles at 0.05 C and 0.1 C-rate, the full cells were cycled at 0.2 C-rate within a voltage range of 2.8–4.25 V.

4.4 Characterization

For postmortem characterizations, the cycled cells were disassembled in an argon-filled glove box immediately after the final delithiation step. Dry-processed anodes, categorized by the FEC content in the electrolyte, were carefully extracted and rinsed with diethyl carbonate (DEC) to remove residual salts. Surface and cross-sectional morphologies were examined using field-emission scanning electron microscopy (FE-SEM, SU8220, Hitachi). Cross-sectional samples were prepared with a cross-sectional ion polisher (IB-09020CP, JEOL). Elemental mapping was conducted using energy-dispersive X-ray spectroscopy (EDS, Ultim Extreme, Oxford) integrated with the SEM. X-ray photoelectron spectroscopy (XPS, NEXSA, Thermo Fisher Scientific) was employed to investigate surface chemical states and bonding environments, with a particular focus on the F 1s region. High-resolution transmission electron microscopy (HRTEM; Cs-corrected TEM, Titan Themis Z, Thermo Scientific) was utilized to observe the solid electrolyte interphase (SEI) formed after the first cycle. To further explore PTFE decomposition as influenced by FEC concentration, additional electrodes with elevated PTFE content (Si/C–graphite : Super-P : PTFE = 4 : 1 : 5 by weight) were fabricated. The crystallinity and structural integrity of PTFE were characterized by X-ray diffraction (XRD, D8 ADVANCE, BRUKER) and Raman spectroscopy (LabRAM Aramis, Horiba Jobin Yvon). Additionally, depth-resolved chemical profiling was performed using time-of-flight secondary ion mass spectrometry (ToF-SIMS, TOF-SIMS5) to assess the elemental distribution as a function of depth.

Author contributions

Seungmin Han: conceptualization, formal analysis, investigation, and writing – original draft. Woojin Jeong: formal analysis, and methodology, and writing – original draft. Ryeowon Kang: data curation and validation. Minseok Kim: data curation and visualization. Mikang Jeong: data curation and visualization. Hyun-Wook Lee: validation. Ye-Jin An: visualization. Ho-Jeong Ji: visualization. Moonsu Yoon: visualization. Patrick Joohyun Kim: methodology. Seho Sun: validation. Taeseup

Song: methodology and visualization. Dongsoo Lee: supervision, and review & editing. Won-Jin Kwak: supervision, conceptualization, writing – original draft, and review & editing. Junghyun Choi: conceptualization, supervision, and writing – original draft, and review & editing.

Conflicts of interest

There are no conflicts to declare.

Data availability

The data supporting this article have been included as part of the SI.

Supplementary information is available. See DOI: **https://doi.org/10.1039/d5eb00100e**.

Acknowledgements

This research was supported by the Industrial Strategic Technology Development Program (grant no. 2410002318, 2410004407 and 2410002516) funded by the Ministry of Trade, Industry & Energy (MOTIE, Korea).

References

1 Afifa, K. Arshad, N. Hussain, M. H. Ashraf and M. Z. Saleem, *Sci. Total Environ.*, 2024, **928**, 172370.
2 V. Foster, P. A. Trotter, S. Werner, M. Niedermayer, Y. Mulugetta, P. Achakulwisut, A. Brophy, N. K. Dubash, S. Fankhauser, A. Hawkes, S. Hirmer, S. Jenkins, S. Loni, A. McGivern, K. Nanthavong, B. Probst, S. Pye, V. Russo, G. Semieniuk, C. Shenga, V. Sridharan, S. Srivastav, Y. Sokona, L. S. Croxatto and P. Yang, *Nat. Energy*, 2024, **9**, 242–250.
3 N. O. Bonsu, *J. Cleaner Prod.*, 2020, **256**, 120659.
4 A. Song, Z. Dan, S. Zheng and Y. Zhou, *Nat. Commun.*, 2024, **15**, 5905.
5 J. Wang, Y. Lyu, R. Zeng, S. Zhang, K. Davey, J. Mao and Z. Guo, *Energy Environ. Sci.*, 2024, **17**, 867–884.
6 W. B. Hawley and J. Li, *J. Energy Storage*, 2019, **25**, 100862.
7 Y. Liu, Y. Zhu and Y. Cui, *Nat. Energy*, 2019, **4**, 540–550.
8 A. K. M. A. Habib, M. K. Hasan, G. F. Issa, D. Singh, S. Islam and T. M. Ghazal, *Batteries*, 2023, **9**, 152.
9 L. Cheah, *Nat. Energy*, 2021, **6**, 17–18.
10 J. Lu, D. Li and L. Ci, *Matter*, 2024, **7**, 4143–4145.
11 Y.-X. Yao, L. Xu, C. Yan and Q. Zhang, *EES Batteries*, 2025, **1**, 9–22.
12 Y. Lu, C.-Z. Zhao, H. Yuan, J.-K. Hu, J.-Q. Huang and Q. Zhang, *Matter*, 2022, **5**, 876–898.
13 N. Kim, Y. Kim, J. Sung and J. Cho, *Nat. Energy*, 2023, **8**, 921–933.
14 K. Feng, M. Li, W. Liu, A. G. Kashkooli, X. Xiao, M. Cai and Z. Chen, *Small*, 2018, **14**, 1702737.
15 D. Lee, S. Lee, D. Jung, K. Roh, J. Seo, J. Kim, K. Kim, P. Joohyun Kim and J. Choi, *Appl. Surf. Sci.*, 2024, **661**, 160023.
16 A. L. Michan, G. Divitini, A. J. Pell, M. Leskes, C. Ducati and C. P. Grey, *J. Am. Chem. Soc.*, 2016, **138**, 7918–7931.
17 M. Ge, C. Cao, G. M. Biesold, C. D. Sewell, S.-M. Hao, J. Huang, W. Zhang, Y. Lai and Z. Lin, *Adv. Mater.*, 2021, **33**, 2004577.
18 K. Cheng, S. Tu, B. Zhang, W. Wang, X. Wang, Y. Tan, X. Chen, C. Li, C. Li, L. Wang and Y. Sun, *Energy Environ. Sci.*, 2024, **17**, 2631–2641.
19 J. Song, S. Ke, P. Sun, D. Yang, C. Luo, Q. Tian, C. Liang and J. Chen, *Nanoscale*, 2023, **15**, 13790–13808.
20 J. Wu, Y. Cao, H. Zhao, J. Mao and Z. Guo, *Carbon Energy*, 2019, **1**, 57–76.
21 K. Sun, X. Li, K. Fu, Z. Zhang, A. Wang, X. He, L. Gong and P. Tan, *EES Batteries*, 2025, **1**, 250–259.
22 M. J. Kim, I. Lee, J. W. Lee, D. Yoon, J. H. Kim, S. Lee, K. Kim, P. J. Kim, J. Choi, Y. C. Kang and D. S. Jung, *Small*, 2024, **20**, 2405005.
23 J. Kim, K. Park, M. Kim, H. Lee, J. Choi, H. B. Park, H. Kim, J. Jang, Y.-H. Kim, T. Song and U. Paik, *Adv. Energy Mater.*, 2024, **14**, 2303455.
24 K. Kwon, J. Kim, S. Han, J. Lee, H. Lee, J. Kwon, J. Lee, J. Seo, P. J. Kim, T. Song and J. Choi, *Small Sci.*, 2024, **4**, 2300302.
25 W. Yao, M. Chouchane, W. Li, S. Bai, Z. Liu, L. Li, A. X. Chen, B. Sayahpour, R. Shimizu, G. Raghavendran, M. A. Schroeder, Y.-T. Chen, D. H. S. Tan, B. Sreenarayanan, C. K. Waters, A. Sichler, B. Gould, D. J. Kountz, D. J. Lipomi, M. Zhang and Y. S. Meng, *Energy Environ. Sci.*, 2023, **16**, 1620–1630.
26 J. Lee, C. Y. Son, S. Han, S. Yang, P. J. Kim, D. Lee, J. W. Lee, W.-H. Ryu and J. Choi, *Chem. Eng. J.*, 2025, **503**, 158271.
27 Q. Wu, J. P. Zheng, M. Hendrickson and E. J. Plichta, *MRS Adv.*, 2019, **4**, 857–863.
28 T. Lee, J. An, W. J. Chung, H. Kim, Y. Cho, H. Song, H. Lee, J. H. Kang and J. W. Choi, *ACS Appl. Mater. Interfaces*, 2024, **16**, 8930–8938.
29 Z. Wei, D. Kong, L. Quan, J. He, J. Liu, Z. Tang, S. Chen, Q. Cai, R. Zhang, H. Liu, K. Xu, L. Xing and W. Li, *Joule*, 2024, **8**, 1350–1363.
30 S. Han, E.-H. Noh, S. Chae, K. Kwon, J. Lee, J.-S. Woo, S. Park, J. W. Lee, P. J. Kim, T. Song, W.-J. Kwak and J. Choi, *J. Energy Storage*, 2024, **96**, 112693.
31 J. Tan, J. Matz, P. Dong, J. Shen and M. Ye, *Adv. Energy Mater.*, 2021, **11**, 2100046.
32 X. He, Z. Jiang, O. U. Akakuru, J. Li and A. Wu, *Chem. Commun.*, 2021, **57**, 12417–12435.
33 C. Zhan, T. Wu, J. Lu and K. Amine, *Energy Environ. Sci.*, 2018, **11**, 243–257.
34 N. Xu, Y. Sun, J. Shi, J. Chen, G. Liu, K. Zhou, H. He, J. Zhu, Z. Zhang and Y. Yang, *J. Power Sources*, 2021, **511**, 230437.
35 S. She, Y. Zhou, Z. Hong, Y. Huang and Y. Wu, *ACS Appl. Energy Mater.*, 2023, **6**, 7289–7297.

36 J. Langdon and A. Manthiram, *Adv. Mater.*, 2022, **34**, 2205188.
37 J.-G. Han, M.-Y. Jeong, K. Kim, C. Park, C. H. Sung, D. W. Bak, K. H. Kim, K.-M. Jeong and N.-S. Choi, *J. Power Sources*, 2020, **446**, 227366.
38 H. Yamane, T. Inoue, M. Fujita and M. Sano, *J. Power Sources*, 2001, **99**, 60–65.
39 X. Wu, Z. Wang, X. Li, H. Guo, Y. Zhang and W. Xiao, *J. Power Sources*, 2012, **204**, 133–138.
40 Z. Dai, Z. Li, R. Chen, F. Wu and L. Li, *Nat. Commun.*, 2023, **14**, 8087.
41 G. Li, R. Xue and L. Chen, *Solid State Ionics*, 1996, **90**, 221–225.
42 Y. Suh, J. K. Koo, H.-j. Im and Y.-J. Kim, *Chem. Eng. J.*, 2023, **476**, 146299.
43 Y. Li, F. Lian, L. Ma, C. Liu, L. Yang, X. Sun and K. Chou, *Electrochim. Acta*, 2015, **168**, 261–270.
44 X. Peng, H. Shen, K. Su, W. Wang, S. Weng, C. Tang, Z. Xue and Y. Xiang, *ACS Appl. Mater. Interfaces*, 2024, **16**, 34281–34293.
45 X. Wang, Z. Zeng, H. Zhang, M. Qin, Y. Zhu and J. Xie, *Chem. Commun.*, 2023, **59**, 12919–12922.
46 Y. Chen, W. Zhao, Q. Zhang, G. Yang, J. Zheng, W. Tang, Q. Xu, C. Lai, J. Yang and C. Peng, *Adv. Funct. Mater.*, 2020, **30**, 2000396.
47 Z. Ren, H. Qiu, C. Fan, S. Zhang, Q. Zhang, Y. Ma, L. Qiao, S. Wang, G. Xu, Z. Cui and G. Cui, *Adv. Funct. Mater.*, 2023, **33**, 2302411.
48 Y. H. T. Tran, J. Han and S.-W. Song, *J. Electrochem. Soc.*, 2021, **168**, 020529.
49 Y. Han, Y. Zhang, Y. Lei, D. Xiao, J. Ni, W. Lin, P. Ming, C. Zhang and Q. Xiao, *Adv. Funct. Mater.*, 2023, **33**, 2301642.
50 Y. Kim, *J. Mater. Sci.*, 2013, **48**, 8547–8551.